Theoretical Analysis of the Aerodynamic Stability of Multiple, Interdigitated Helical Vortices

B. P. GUPTA*
Bell Helicopter Company, Fort Worth, Texas
AND
R. G. LOEWY†
University of Rochester, Rochester, N.Y.

A small perturbation stability analysis of a doubly infinite array of interdigitated, right circular helical vortices has been formulated. This array corresponds to the vortices trailed from the tips of the blades of a helicopter rotor or propeller in static thrust or axial flight condition and at great distance from the plane of rotation of the blades. A continuum of instability modes has been found associated with all values of wave numbers; only modes with wave numbers 0 and 1 are so much as neutrally stable, and for the case of a single helix. The most unstable modes involve the most axial motion of adjacent vortex segments relative to each other. Maximum divergence rates increase as the helix pitch decreases, increase as the number of helices increase and decrease as the number of cycles of deformations in one turn of the helix (i.e., wave number) increases. The helix filament core diameter can have substantial effect on the stability of a single helix, but not for multiple arrays. The larger the core diameter, the more sensitive the analysis is to the means by which the singularities in the self-induction integrals are eliminated. Increasing core diameters reduces the maximum divergence rates in all cases.

Introduction

THE geometry of the wake beneath a helicopter rotor is important to the accurate prediction of the airloads acting on the blades in many flight conditions. Determination of such airloads is prerequisite to nearly every area of rotary wing design, including performance, vibrations, acoustics, and structural integrity. The impact of wake geometry is felt directly in attempts to predict wake induced velocity fields. Inability to do so with acceptable accuracy has limited the state-of-the-art of helicopter rotor design for perhaps a decade. This is a problem on which considerable emphasis has been and still is being placed. Generally, the objective is to develop a rotary wing equivalent to the classical lifting line type analysis employed with success for fixed-wing aircraft. Some of the most promising methods of wake analysis are those which deal with the three-dimensional array of vorticity in the wake which is trailed in the tangential and shed in the radial directions from the finite number of blades in a lifting rotor. Since the former has large steady components, while the latter is purely oscillatory, the wake induced field of a hovering rotor can for many purposes be inferred from proper consideration of just the trailing vorticity; e.g., a set of interdigitated circular vortex helices generated by the tip of each blade in the rotor.

Such a classical representation of the wake can generally be divided into two distinct parts, near wake and far wake. The near wake can effectively be represented by circular helices trailing from the blade tip together with the "lifting line" or bound vortex representation of the rotor blades. For some purposes it may be necessary to consider a root vortex as well. The far wake can be treated as consisting of an array of infinitely long, interdigitated circular helices as generated by the blade tip only.

Received September 24, 1973; revision received March 22, 1974. This research was partially supported by a contract from U.S. Army Air Mobility Research and Development Lab. under Contract DAAJ02-72-C-0042.

Index category: Rotary Wing Aerodynamics.

* Research Engineer; formerly Graduate Student, University of Rochester, Rochester, N.Y.

† Professor and Dean of College of Engineering. Member AIAA.

In classical inflow wake analysis methods, the wake geometry is prescribed in advance. This prescription imposes a fundamental limit to such methods and optimum rotor designs are not likely to be achieved until distortions in the wake can be accounted for rather than a rigid prescribed geometry. Flow visualization as well as numerical integration and iteration techniques have revealed that the actual rotor wake geometry differs significantly from a pure helix. Landgrebe,[1] by means of flow visualization as well as distorted wake geometry calculations, noted that the portion of the wake in the immediate vicinity of the rotor plane in his studies converged to a reasonably stable configuration while the wake became unstable at moderate distances from the rotor. It therefore appears that valuable insight as to the extent the distortions of the trailed vortices must be accounted for to achieve acceptable theoretical rotor blade analysis methods will be gained by studying the stability of the wakes. Furthermore, it seems prudent to examine the far wake first, both because of its greater simplicity and because of its apparently greater tendencies toward instability. Two-dimensional flowfields behind a circular cylinder were found by Kármán[2] to be stable only when vortices were in the staggered formation which has come to be known as the "Kármán Vortex Street." An interdigitated vortex helix array such as might represent the wake of a multi-bladed rotor can be thought of as a rotary analog of the "Kármán Vortex Street" and analyzed for stability in a similar manner. At high Reynolds number the three-dimensional flow in the wake of a circular disk with its polar axis parallel to the flow has been found to consist of a rotating helical vortex filament. This prompted an early stability analysis of a single helical vortex by Levy and Forsdyke.[3] Their work, while basically like that of Kármán, contains some erroneous conclusions, as explained subsequently. Another study of a single helical vortex was published by Widnall[4] after the initiation of the research reported here; a comparison of the Widnall results with those obtained here is contained in subsequent parts of this paper.

The present analysis deals with the stability of centerline displacements of interdigitated helical vortex systems. Centerline perturbation displacements are assumed, and the self-induced and mutually induced perturbation velocities at the perturbed positions are calculated. Subsequently, the vorticity transport theorem is invoked to assure the compatibility of induced

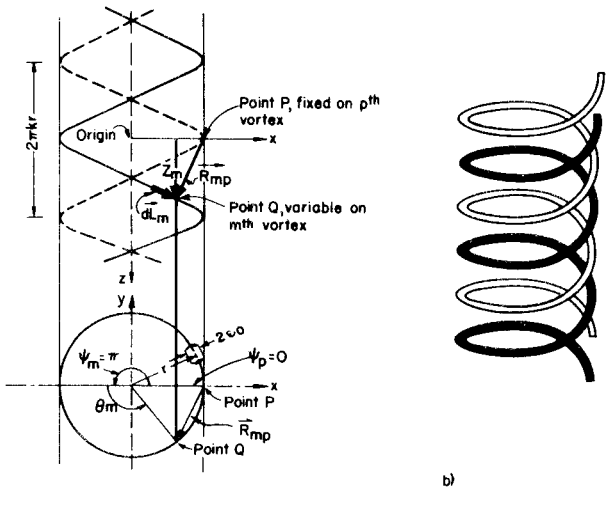

Fig. 1 Undistorted pth and mth vortex helices of radius r, pitch k, and vortex core diameter $2\varepsilon_0$; a) plan and elevation; b) isometric.

velocities and time rates of displacement. This leads to an eigenvalue problem where the complex eigenvalues contain the divergence or subsidence of the perturbation displacements.

Theoretical Development

Consider an array of n coaxial vortices of radius r, and pitch k, and separated azimuthally by an angle ψ_m defined as measured from the first helix. Then

$$\psi_m = \frac{(m-1)2\pi}{n}; \qquad m = 1, 2, \ldots, n$$

The pth and mth vortices are sketched in Fig. 1. If θ_m represents the parameter for the mth vortex, the parametric equation for the mth vortex in Cartesian coordinates can be written as

$$\begin{aligned} x_m &= r\cos(\theta_m + \psi_m) \\ y_m &= r\sin(\theta_m + \psi_m) \\ z_m &= kr\theta_m \end{aligned} \tag{1}$$

The induced velocity $\mathbf{U}_p$ due to a system of n interdigitated vortices, each with circulation strength Γ, at a point $\mathbf{r}_p : (x_p, y_p, z_p)$ on the pth vortex is given by the Biot-Savart Law as

$$\mathbf{U}_p = \sum_{m=1}^{n} \frac{\Gamma}{4\pi} \int \frac{\mathbf{R}_{mp} \times d\mathbf{L}_m}{|\mathbf{R}_{mp}|^3} \tag{2}$$

where $d\mathbf{L}_m$ is the elemental length vector on the mth vortex at point $\mathbf{r}_m : (x_m, y_m, z_m)$ and $\mathbf{R}_{mp}$ is the relative position vector of the point $\mathbf{r}_m$ on the mth vortex relative to the point $\mathbf{r}_p$ on the pth vortex; i.e., $\mathbf{R}_{mp} = \mathbf{r}_m - \mathbf{r}_p$. The first vector in the difference is always associated with a point involved in the space integration, while the second is associated with the specific point at which the induced velocity is being evaluated. To avoid confusion where $m = p$, i.e., when integrating over the vortex on which, at some point, the induced velocity is being calculated, a prime will be used on $\mathbf{r}_m$ and its components. Denoting $\theta_m' - \theta_p$ by x and $\psi_m - \psi_p$ by ψ_{mp}, the velocity components of the undistorted helix can be written from Eq. (2) in cylindrical polar coordinates (for details, see Ref. 5) as

$$\begin{aligned} (\mathbf{U}_p \cdot \mathbf{e}_r) &= \sum_{m=1}^{n} \frac{\Gamma}{4\pi} \int_{-\infty}^{\infty} \frac{kr^2[\sin(x+\psi_{mp}) - x\cos(x+\psi_{mp})]}{[2r^2 - 2r^2\cos(x+\psi_{mp}) + k^2r^2x^2]^{3/2}}\, dx \\ (\mathbf{U}_p \cdot \mathbf{e}_\phi) &= \sum_{m=1}^{n} \frac{\Gamma}{4\pi} \int_{-\infty}^{\infty} \frac{kr^2[1 - \cos(x+\psi_{mp}) - x\sin(x+\psi_{mp})]}{[2r^2 - 2r^2\cos(x+\psi_{mp}) + k^2r^2x^2]^{3/2}}\, dx \\ (\mathbf{U}_p \cdot \mathbf{e}_z) &= \sum_{m=1}^{n} \frac{\Gamma}{4\pi} \int_{-\infty}^{\infty} \frac{r^2[1 - \cos(x+\psi_{mp})]}{[2r^2 - 2r^2\cos(x+\psi_{mp}) + k^2r^2x^2]^{3/2}}\, dx \end{aligned} \tag{3}$$

To obtain the perturbation equations, let the point (x_m', y_m', z_m') on the mth vortex helix as defined in Eq. (1) be distorted to $(x_m' + \delta x_m', y_m' + \delta y_m', z_m' + \delta z_m')$ where $\delta x_m', \delta y_m', \delta z_m'$ are functions of the parameter θ_m' and time t, and are small first order. Denoting the vector $(\delta x_m', \delta y_m', \delta z_m')$ by $\delta\mathbf{r}_m'$, the induced velocity $\mathbf{U}_p$ at the point $\mathbf{r}_p + \delta\mathbf{r}_p$ associated with the distorted system of vortex helices is given by the Biot-Savart Law as

$$\mathbf{U}_p(\mathbf{r}_p + \delta\mathbf{r}_p) = \sum_{m=1}^{n} \frac{\Gamma}{4\pi} \int \frac{\mathbf{R}_{mp} \times d\mathbf{L}_m(\mathbf{r}_m' + \delta\mathbf{r}_m')}{|\mathbf{R}_{mp}|^3} \tag{4}$$

where now

$$\begin{aligned} \mathbf{R}_{mp} &= \mathbf{r}_m' - \mathbf{r}_p + \delta\mathbf{r}_m' - \delta\mathbf{r}_p \\ d\mathbf{L}_m &= [dx_m' + d(\delta x_m'),\ dy_m' + d(\delta y_m'),\ dz_m' + d(\delta z_m')] \end{aligned}$$

Equation (4) can be separated into two parts: one containing zero-order terms and the other first-order terms. We define the following two quantities:

$$\begin{aligned} J_{mp} &\triangleq (x_m' - x_p)^2 + (y_m' - y_p)^2 + (z_m' - z_p)^2 \\ K_{mp} &\triangleq (x_m' - x_p)(\delta x_m' - \delta x_p) + (y_m' - y_p)(\delta y_m' - \delta y_p) + \\ &\qquad (z_m' - z_p)(\delta z_m' - \delta z_p) \end{aligned}$$

Now in terms of J_{mp} and K_{mp}, and dropping higher terms

$$\begin{aligned} |\mathbf{R}_{mp}|_0^{-3} &= J_{mp}^{-3/2} \\ |\mathbf{R}_{mp}|_1^{-3} &= -3J_{mp}^{-5/2}K_{mp} \end{aligned}$$

The zero-order terms in Eq. (4) are the steady velocity expressions which were given in Eq. (3) in cylindrical polar coordinates. The first-order terms in Eq. (4) can be written

$$\begin{aligned} [\delta\mathbf{U}_p] = &\sum_{m=1}^{n} \frac{\Gamma}{4\pi} \int_{\theta_m' = -\infty}^{\theta_m' = +\infty} J_{mp}^{-3/2} \left[(\mathbf{r}_m' - \mathbf{r}_p) \times \right. \\ &\left. \frac{\partial}{\partial\theta_m'}(\delta\mathbf{r}_m') + (\delta\mathbf{r}_m' - \delta\mathbf{r}_p) \times \frac{\partial}{\partial\theta_m'}(\mathbf{r}_m') \right] d\theta_m' + \\ &\sum_{m=1}^{n} \frac{\Gamma}{4\pi} \int_{\theta_m' = -\infty}^{\theta_m' = +\infty} -3K_{mp}J_{mp}^{-5/2} \left[(\mathbf{r}_m' - \mathbf{r}_p) \times \right. \\ &\left. \frac{\partial}{\partial\theta_m'}(\mathbf{r}_m') \right] d\theta_m' \end{aligned} \tag{5}$$

where $\delta\mathbf{U}_p$ is the first-order induced velocity at the point $(\mathbf{r}_p + \delta\mathbf{r}_p)$ of the pth vortex.

The vorticity transport theorem (see, for example, Ref. 6) states that elements of a vortex line move with the fluid particles. If one considers the fluid velocities which are induced by the vortices, then the vorticity transport theorem can be expressed simply as $(d/dt)(\mathbf{r}) = \mathbf{U}$ for all the points $\mathbf{r}$ on the undeformed vortex filaments. The vorticity transport theorem for the perturbed system of vortices can be stated as

$$\frac{d}{dt}(\mathbf{r}_p + \delta\mathbf{r}_p) = \mathbf{U}_p(\mathbf{r}_p + \delta\mathbf{r}_p) \tag{6}$$

The right-hand side of Eq. (6) is obtained by making use of Eq. (4). The Cartesian components of the left-hand side terms are evaluated in the following manner:

$$\begin{aligned} x_p + \delta x_p &= r\cos(\theta_p + \psi_p) + \delta r_p\cos(\theta_p + \psi_p) - \\ &\qquad r\sin(\theta_p + \psi_p)\,\delta\phi_p \\ \frac{d}{dt}(x_p + \delta x_p) &= \dot{r}_p\cos(\theta_p + \psi_p) - r\sin(\theta_p + \psi_p)\dot{\phi}_p + \\ &\qquad \delta\dot{r}_p\cos(\theta_p + \psi_p) - \\ &\qquad \delta r_p\sin(\theta_p + \psi_p)\dot{\phi}_p - \dot{r}_p\sin(\theta_p + \psi_p)\,\delta\phi_p - \\ &\qquad r\cos(\theta_p + \psi_p)\dot{\phi}_p\,\delta\phi_p - r\sin(\theta_p + \psi_p)\,\delta\dot{\phi}_p \end{aligned} \tag{7}$$

Similarly for $y_p + \delta y_p$ and $z_p + \delta z_p$. The terms δr_p, $\delta\phi_p$, and δz_p represent first-order perturbations in the r, ϕ, and z directions, respectively, and $\delta\dot{r}_p$, $\delta\dot{\phi}_p$, and $\delta\dot{z}_p$ are the corresponding time derivatives. The terms $\dot{r}_p$, $r\,\delta\dot{\phi}_p$, and $\delta\dot{z}_p$ are the zero-order velocity components in cylindrical polar coordinates.

The right-hand side of Eq. (6) is expressed in terms of Cartesian coordinates as can be seen from Eq. (4). This is

transformed to cylindrical polar coordinates using the following transformation matrix

$$\begin{bmatrix} \delta r \\ r\,\delta\phi \\ \delta z \end{bmatrix} = \begin{bmatrix} \cos(\theta_p+\psi_p+\delta\phi_p) & \sin(\theta_p+\psi_p+\delta\phi_p) & 0 \\ -\sin(\theta_p+\psi_p+\delta\phi_p) & \cos(\theta_p+\psi_p+\delta\phi_p) & 0 \\ 0 & 0 & 1 \end{bmatrix} \begin{bmatrix} \delta x \\ \delta y \\ \delta z \end{bmatrix}$$

The Cartesian components of the left-hand side of Eq. (6) are also transformed using the same transformation Eqs. (7). Using Eq. (6), so transformed, the first-order perturbation equations can be written as

$$\delta\dot{r}_p = \sum_{m=1}^{n} \frac{\Gamma}{4\pi} \int_{-\infty}^{\infty} J_{mp}{}^{-3/2} \Big[kr \Big\{ -x\sin(x+\psi_{mp}) \frac{\partial}{\partial\theta_m{}'}(\delta r_m') - x\cos(x+\psi_{mp})\,\delta r_m' + \sin(x+\psi_{mp})\,\delta r_m' \Big\} + kr^2 \Big\{ \cos(x+\psi_{mp})\,\delta\phi_m' + x\sin(x+\psi_{mp})\,\delta\phi_m' - x\cos(x+\psi_{mp}) \frac{\partial}{\partial\theta_m{}'}(\delta\phi_m') \Big\} + kr^2\,\delta\hat{\phi}_p\{-\cos(x+\psi_{mp})\} + r \Big\{ -\delta z_m'\cos(x+\psi_{mp}) + \delta z_p\cos(x+\psi_{mp}) + \sin(x+\psi_{mp}) \frac{\partial}{\partial\theta_m{}'}(\delta z_m') \Big\} \Big] dx - 3\sum_{m=1}^{n} \frac{\Gamma}{4\pi} \int_{-\infty}^{\infty} J_{mp}{}^{-5/2} kr^2 \{\sin(x+\psi_{mp}) - x\cos(x+\psi_{mp})\} K_{mp}\,dx$$

$$r\,\delta\dot{\phi}_p = \sum_{m=1}^{n} \frac{\Gamma}{4\pi} \int_{-\infty}^{\infty} J_{mp}{}^{-3/2} \Big[kr \Big\{ x\cos(x+\psi_{mp}) \frac{\partial}{\partial\theta_m{}'}(\delta r_m') - \cos(x+\psi_{mp})\,\delta r_m' - x\sin(x+\psi_{mp})\,\delta r_m' + \cos(x+\psi_{mp})\,\delta r_p + x\sin(x+\psi_{mp})\,\delta r_p \Big\} + kr^2 \Big\{ -x\sin(x+\psi_{mp}) \frac{\partial}{\partial\theta_m{}'}(\delta\phi_m') - x\cos(x+\psi_{mp})\,\delta\phi_m' + \sin(x+\psi_{mp})\,\delta\phi_m' - \sin(x+\psi_{mp})\,\delta\phi_p + x\cos(x+\psi_{mp})\,\delta\phi_p \Big\} + r \Big\{ -\sin(x+\psi_{mp})\,\delta z_m' + \sin(x+\psi_{mp})\,\delta z_p - \cos(x+\psi_{mp}) \frac{\partial}{\partial\theta_m{}'}(\delta z_m') + \frac{\partial}{\partial\theta_m{}'}(\delta z_m') \Big\} \Big] dx - 3\sum_{m=1}^{n} \frac{\Gamma}{4\pi} \int_{-\infty}^{\infty} J_{mp}{}^{-5/2} kr^2 \{1 - \cos(x+\psi_{mp}) - x\sin(x+\psi_{mp})\} K_{mp}\,dx$$

$$\delta\dot{z}_p = \sum_{m=1}^{n} \frac{\Gamma}{4\pi} \int_{-\infty}^{\infty} J_{mp}{}^{-3/2} \Big[r \Big\{ \frac{\partial}{\partial\theta_m{}'}(\delta r_m')\sin(x+\psi_{mp}) + 2\delta r_m' - \delta r_m'\cos(x+\psi_{mp}) - \delta r_p\cos(x+\psi_{mp}) \Big\} + r^2 \Big\{ \frac{\partial}{\partial\theta_m{}'}(\delta\phi_m') + \delta\phi_m'\sin(x+\psi_{mp}) - \cos(x+\psi_{mp}) \frac{\partial}{\partial\theta_m{}'}(\delta\phi_m') - \delta\phi_p\sin(x+\psi_{mp}) \Big\} \Big] dx - 3\sum_{m=1}^{n} \frac{\Gamma}{4\pi} \int_{-\infty}^{\infty} J_{mp}{}^{-5/2} r^2 \{1 - \cos(x+\psi_{mp})\} K_{mp}\,dx$$

These integro-differential perturbation equations admit solutions of the exponential type, for perturbations $\delta\mathbf{r}_m$. The first-order perturbation vector $\boldsymbol{\delta}\mathbf{r}_m$ and its components are thus assumed to be

$$\boldsymbol{\delta}\mathbf{r}_m = \boldsymbol{\delta}\hat{\mathbf{r}}_m\, e^{\alpha t + i\omega\theta_m'} \tag{8}$$

where $\delta\mathbf{r}_m$ = vector perturbation of the mth vortex having δr_m, $\delta\phi_m$, and δz_m as its components in the r, ϕ, and z directions; $\boldsymbol{\delta}\hat{\mathbf{r}}_m$ = vector perturbation amplitude of $\delta\mathbf{r}_m$ having components $\delta\hat{r}_m$, $\delta\hat{\phi}_m$, and $\delta\hat{z}_m$; α = exponential growth rate factor, complex; and ω = perturbation wave number. Note that

$$\frac{\partial}{\partial\theta_m{}'}(\delta\mathbf{r}_m) = i\omega\,\boldsymbol{\delta}\mathbf{r}_m \tag{9}$$

Remembering that $x = \theta_m' - \theta_p$, $\delta\mathbf{r}_m$ can also be written as $\boldsymbol{\delta}\mathbf{r}_m = \boldsymbol{\delta}\hat{\mathbf{r}}_m \cdot e^{\alpha t + i\omega\theta_p} \cdot e^{i\omega x}$. This will allow dividing the whole equation by the quantity $e^{\alpha t + i\omega\theta_p}$.

In principle, no generality is lost in considering such solutions, since an arbitrary perturbation can be synthesized from these by Fourier Integration. In practice, the numerical work will, of course, deal with a limited number of wavelengths.

Inserting solutions of the type shown in Eqs. (8) and (9) into the first-order perturbation equations leads to the following eigenvalue equations:

$$\frac{4\pi\alpha\,\delta\hat{r}_p}{\Gamma} = \sum_{m=1}^{n} \int_{-\infty}^{\infty} J_{mp}{}^{-3/2} \Big[kr\,e^{i\omega x}\,\delta\hat{r}_m \{ -i\omega x\sin(x+\psi_{mp}) - x\cos(x+\psi_{mp}) + \sin(x+\psi_{mp}) \} + kr^2\,e^{i\omega x}\,\delta\hat{\phi}_m \{ \cos(x+\psi_{mp}) + x\sin(x+\psi_{mp}) - i\omega x\cos(x+\psi_{mp}) \} + r\,e^{i\omega x}\,\delta\hat{z}_m \{ -\cos(x+\psi_{mp}) + i\omega\sin(x+\psi_{mp}) \} + kr^2\,\delta\hat{\phi}_p \{ -\cos(x+\psi_{mp}) - x\sin(x+\psi_{mp}) \} + r\,\delta\hat{z}_p\cos(x+\psi_{mp}) \Big] dx - 3\sum_{m=1}^{n} \int_{-\infty}^{\infty} J_{mp}{}^{-5/2} K_{mp} \Big[kr^2 \{ \sin(x+\psi_{mp}) - x\cos(x+\psi_{mp}) \} \Big] dx \tag{10}$$

$$\frac{4\pi\alpha r\,\delta\hat{\phi}_p}{\Gamma} = \sum_{m=1}^{n} \int_{-\infty}^{\infty} J_{mp}{}^{-3/2} \Big[kr\,\delta\hat{r}_m\,e^{i\omega x} \{ i\omega x\cos(x+\psi_{mp}) - \cos(x+\psi_{mp}) - x\sin(x+\psi_{mp}) \} + kr^2\,\delta\hat{\phi}_m\,e^{i\omega x} \{ -i\omega x\sin(x+\psi_{mp}) - x\cos(x+\psi_{mp}) + \sin(x+\psi_{mp}) \} + r\,\delta\hat{z}_m\,e^{i\omega x} \{ -\sin(x+\psi_{mp}) - i\omega\cos(x+\psi_{mp}) + i\omega \} + kr\,\delta\hat{r}_p \{ \cos(x+\psi_{mp}) + x\sin(x+\psi_{mp}) \} + kr^2\,\delta\phi_p \{ x\cos(x+\psi_{mp}) - \sin(x+\psi_{mp}) \} + \sin(x+\psi_{mp})\,\delta\hat{z}_p \Big] dx - 3\sum_{m=1}^{n} \int_{-\infty}^{\infty} J_{mp}{}^{-5/2} \Big[kr^2 \{ 1 - \cos(x+\psi_{mp}) - x\sin(x+\psi_{mp}) \} \Big] K_{mp}\,dx \tag{11}$$

$$\frac{4\pi\alpha\,\delta\hat{z}_p}{\Gamma} = \sum_{m=1}^{n} \int_{-\infty}^{\infty} J_{mp}{}^{-3/2} \Big[r\,\delta\hat{r}_m\,e^{i\omega x} \{ i\omega\sin(x+\psi_{mp}) + 2 - \cos(x+\psi_{mp}) \} + r^2\,\delta\hat{\phi}_m\,e^{i\omega x} \{ i\omega + \sin(x+\psi_{mp}) - i\omega\cos(x+\psi_{mp}) \} - \delta\hat{r}_p\cos(x+\psi_{mp}) - \delta\hat{\phi}_p\sin(x+\psi_{mp}) \Big] dx - 3\sum_{m=1}^{n} \int_{-\infty}^{\infty} J_{mp}{}^{-5/2} r^2 \{ 1 - \cos(x+\psi_{mp}) \} K_{mp}\,dx \tag{12}$$

where

$$K_{mp} = r\,\delta\hat{r}_m\,e^{i\omega x} \{ 1 - \cos(x+\psi_{mp}) \} + r^2\,\delta\hat{\phi}_m\,e^{i\omega x}\sin(x+\psi_{mp}) + kr\,\delta\hat{z}_m\,x\,e^{i\omega x} + r\,\delta\hat{r}_p \{ 1 - \cos(x+\psi_{mp}) \} - r^2\,\delta\hat{\phi}_p\sin(x+\psi_{mp}) - krx\,\delta\hat{z}_p \tag{13}$$

Equations (10–12) can be written for integer values of m ranging from 1 to n, where n corresponds to the number of interdigitated helices. After numerically evaluating the set of self and mutual induction integrals a system of $3n$ eigenvalue equations is obtained.

Treatment of Singularities and Computations

The integrals in the perturbation equations are convergent, since both $J_{mp}{}^{-3/2}$ and $J_{mp}{}^{-5/2}$ vary as x^{-3} and x^{-5}, respectively, in the limit as x approaches infinity. The term corresponding to $m = p$ in the sum on the right-hand side gives the self-induced components for the pth vortex. For $m = p$, $\psi_{pp} = \psi_p - \psi_p = 0$ and the numerator as well as the denominator become zero at $x = 0$. However, since the denominator goes to zero faster than the numerator, there is a singularity in the line integral. The difficulty is fundamental in that the Biot-Savart Law is invalid within the vortex core, i.e., where viscous forces predominate. If we assume that the vortex has a finite core the size of ε (ratio of vortex core diameter and helix diameter), the singularity in the Biot-Savart integral can be removed in several

possible ways developed to a considerable extent in the literature. S. C. Crow[7] in his work with fixed wing trailing vortices eliminated the singularities by cutting the integral off at some arc length on either side of the point where $|\mathbf{R}_{pp}| = 0$. He determined this cutoff arc length by taking it proportional to the radius of the vortex core and evaluating the constant of proportionality by reference to two similar problems whose solutions are known by other means. More recently Widnall[4] used the method of matched asymptotic expansions to remove the singularity in the self-induction integrals by relating the problem for helices to that for two-dimensional circular vortex rings.

In the present work, the denominator $|\mathbf{R}_{pp}|^3$ has been replaced by $[|\mathbf{R}_{pp}|^2+\varepsilon^2]^{3/2}$. This avoids complications when multiple helices are considered, yet gives equivalent results for the case of single helix considered by Widnall.

The almost singular behavior of self-induction integrals is eliminated by adding and subtracting functions which have the same near-singularities numerically but which can be more easily treated analytically. Consider, for example, one of the integrands, which is of the type

$$J = x\cos x/[2-2\cos x+k^2x^2+\varepsilon^2]^{3/2}$$

For small values of x, J behaves as

$$\frac{x\cdot 1}{[2-2(1-x^2/2)+k^2x^2+\varepsilon^2]^{3/2}} = \frac{(1+k^2)^{-3/2}\cdot x}{[x^2+a^2]^{3/2}}$$

where $a^2 = \varepsilon^2/(1+k^2)$. This integrand will be used to eliminate the near singular behavior near $x = 0$ of the integrand J. The integrand $x/(x^2+a^2)^{3/2}$ can be integrated analytically between finite limits and the limits are from 0 to x_u where x_u is chosen so that the modified integrand is sufficiently smooth.

A combination of two numerical integration methods is used to achieve a balance between the requirements for accuracy and reasonable computer time. Since major contributions to the integrals are made when x is small, a double precision Simpson's rule was used in the range $x = 0$ to $x = 50$. To an upper cutoff limit and beyond, a double precision quadrature integration was employed. The quadrature integration is much faster on the computer, although less accurate. Test programs were run to check the convergence of integrated values. The upper limit and interval size of the Simpson's rule integration, the range of integration of the Gaussian Quadrature Formula, and the upper cutoff limit for the infinite integrals were all varied till computed eigenvalues converged to five-digit accuracy for the range of the parameters investigated.

Since the effect of an arbitrary mth vortex on the pth vortex is dependent only upon the difference $\psi_m-\psi_p = \psi_{mp}$ rather than ψ_m or ψ_p the number of calculations could be reduced from $n\times n$ to $(2n-1)$, each calculation giving either a self-induction or mutual-induction 3×3 matrix. Another reduction in the number of calculations results since integration limits are from $-\infty$ to $+\infty$; the self or mutual induction calculation for phase differences $-\psi_{mp}$ thus result in the same 3×3 matrix as calculations for ψ_{mp}. This simplification further reduces the number of calculations from $(2n-1)$ to n.

The resultant perturbation equations constitute a $3n\times 3n$ eigenmatrix of complex elements. Eigenvalues and right eigenvectors of this complex matrix have been calculated using the QR algorithm and the Wielandt inverse power method for vectors (see, for example, Ref. 8). The function of the QR algorithm is to decompose an arbitrary, nonsymmetric complex matrix A into a product QU, where Q is unitary and U is upper triangular. This method utilizes unitary transformations and tends to be numerically stable. A set of $3n$ eigenvalues result for an n-bladed rotor for specified values of the parameter, ω. Eigenvalues with positive real parts show instability while those with negative real parts show stability. Eigenvalues with zero real parts are neutrally stable. The imaginary parts of the eigenvalues define the direction of propagation of the disturbances.

The stability analysis results obtained in this study indicated that there are in all cases disturbances travelling in several directions with positive, negative, and zero growth rates. In a linear stability analysis such as this, the unstable modes with the largest divergence rates very quickly dominate the disturbance shapes, thus determining the shape of the distorted helices.

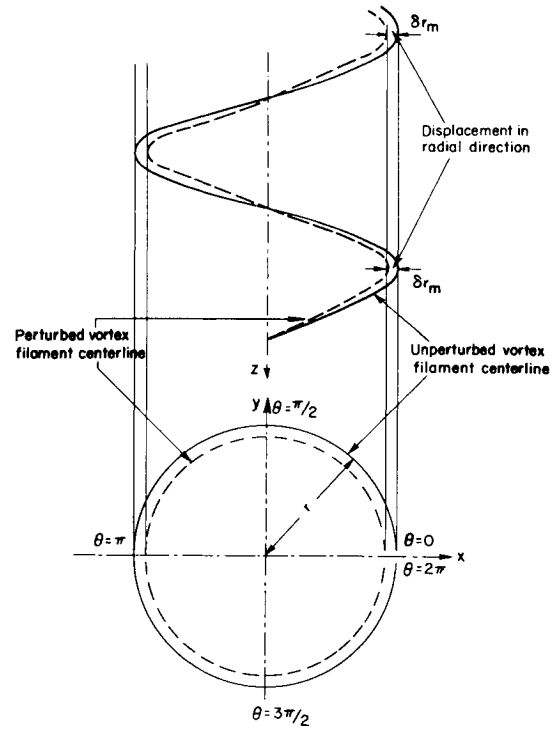

Fig. 2 Radial perturbations in wave number = 0 mode (dilatational).

Results

If D_L is the disk loading and ρ is the air mass density, the average axial velocity in the fully developed slipstream, V_z, is given for a hovering rotor by

$$V_z = (2D_L/\rho)^{1/2}$$

Typical disk loadings in a hovering rotor range from 2 to 10 lb/ft which corresponds to an axial velocity range of 40–95 fps. Typical tip speeds range from 500 to 800 fps and consequently helix pitch varies from 0.05 to 0.20.

Most of the results obtained in the present study are for a pitch value of 0.1. The parameter termed "core size" is the ratio of vortex core diameter to the helix diameter. This parameter has also chosen to be 0.1, although some cases have also been run for a core size of 0.33 to investigate its effect on stability. Perturbation wave numbers have been examined from 0.25 (one distortion cycle for every four turns of the helix; i.e., long wavelengths) to 8.0 (one distortion cycle in $\frac{1}{8}$ of a helix turn; i.e., short wavelengths). Perturbation wavelengths which are very short compared to the helix diameter would seem to involve changes of vortex core cross section in the plane perpendicular to the helical filament centerline. Thomson,[9] however, has shown that so long as the radius of the cross section of the core in the plane perpendicular to the filament centerline is small with respect to the radius of curvature of the centerline, the cross section will remain approximately circular under the self influence of the whole vortex.

A short physical description of modal deflections will provide increased insight into the instability mechanism. For simplicity consider the following perturbations.

$$\delta r = \delta\hat{r}\cos\omega\theta$$

$$\delta\phi = \delta\hat{\phi}\cos\omega\theta$$

$$\delta z = \delta\hat{z}\cos\omega\theta$$

A wave number value of zero ($\omega = 0$) corresponds to dilatation in a radial direction, while the z and ϕ direction

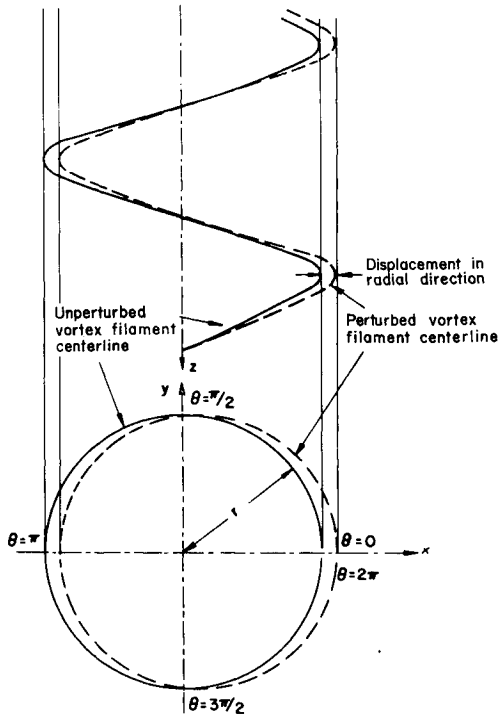

Fig. 3 Radial perturbations in wave number = 1 mode.

perturbations change the position of the given helix with respect to the coordinate axes. These perturbations are depicted in Fig. 2. Since the basic helical shape is maintained, the $\omega = 0$ perturbation might be expected to be neutrally stable for a single helix.

For $\omega = 1$ the radial and axial deformations are plotted in Figs. 3 and 4, respectively. It is seen that the radial deformations

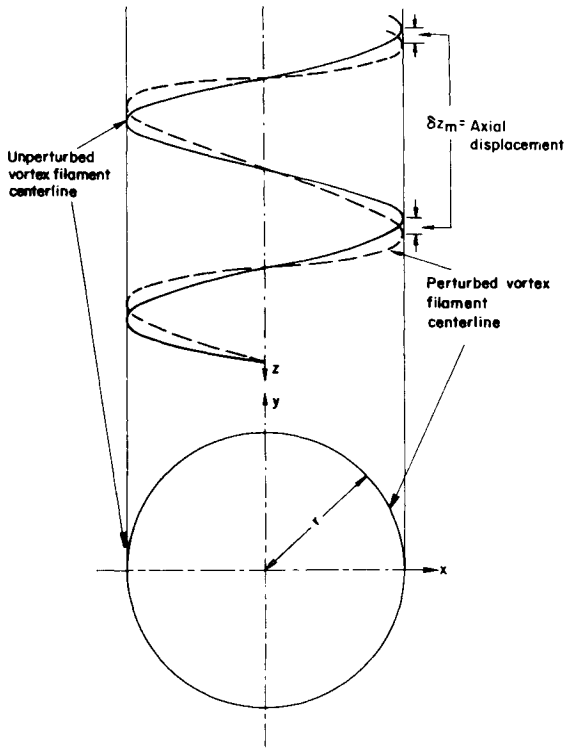

Fig. 4 Axial perturbations in wave number = 1 mode.

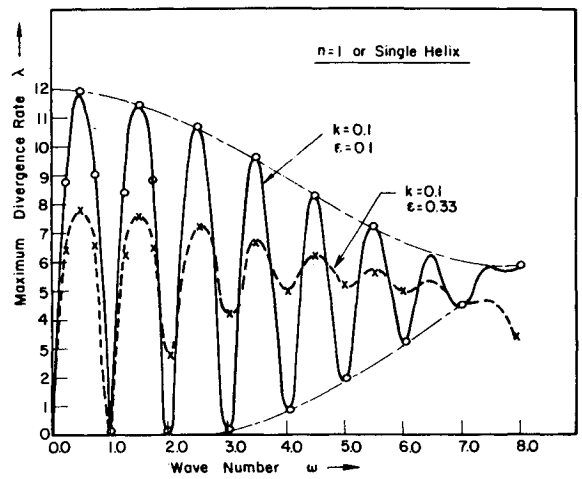

Fig. 5 Plot of maximum divergence rate vs wave number for single helix.

cause a relatively undistorted translation, while the axial deformations amount to a tilting of coils relative to the axis of the helix. Deformations in the ϕ direction mainly stretch or compress the helical vortex lines and such effects have been assumed to be of little consequence in the present analysis. The radial and axial deformations for a wave number of 2 can be similarly sketched and are seen to cause substantial deviations from the helical shape.

For multiple interdigitated helices, each of the vortex helices can undergo the modal deformations described above, but the relative magnitude and phase of these deformations on one helix as compared to the others are determined by the eigensolution. Since the phenomenon can be affected in a major way by interaction among the separate vortex filaments, the inter-

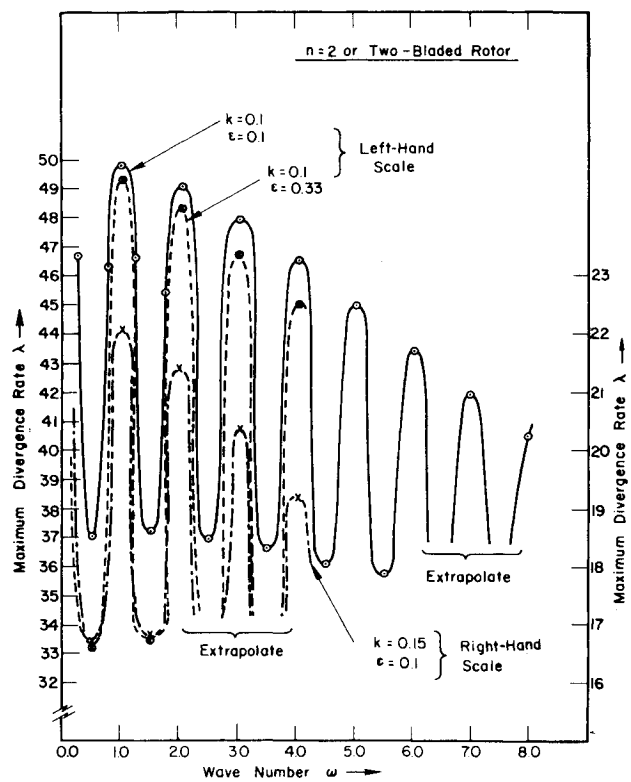

Fig. 6 Plot of maximum divergence rate vs wave number for two-bladed rotor.

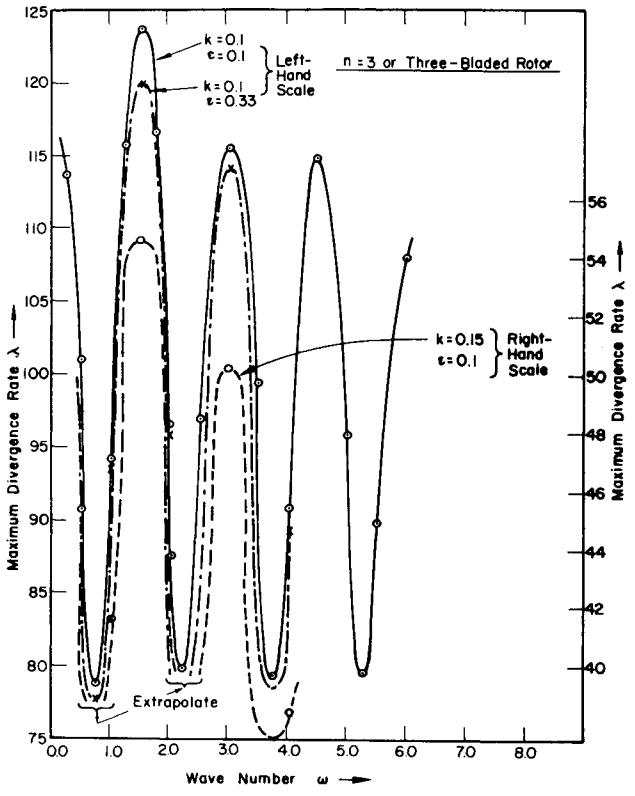

Fig. 7 Plot of maximum divergence rate vs wave number for three-bladed rotor.

digitated system may be highly unstable at wave numbers for which individual helices are neutrally stable.

The representative stability results for a single helix are plotted in Fig. 5 and for two-, three-, and six-bladed rotors in Figs. 6–8. Most of the important conclusions can be made from results shown in Figs. 5–8; however, the results for four- and five-bladed rotors are reported in Ref. 5. In each case the maximum growth rate of perturbations is plotted against the wave numbers. The single helix is neutrally stable for wave numbers 0 and 1 and unstable for all other wave numbers examined; it diverges most rapidly at wave numbers $\frac{1}{2}$, $\frac{3}{2}$, $\frac{5}{2}$, etc., and at the slowest rates at wave numbers 2, 3, 4, etc.

The case of single helix has been examined for stability to help verify the present theory and increase confidence in the numerical methods used in the investigation. The Levy and Forsdyke analysis,[3] carried out in 1928, concluded that a double infinite constant diameter helical vortex is unstable below and stable above a helix pitch angle of 0.3 in the wave number = 1 mode. This is an erroneous conclusion since the perturbation mode $\omega = 1$ is almost the same as a change in the arbitrary choice of a coordinate axis system, and should therefore be expected to be neutrally stable. The stability analysis of a single helical vortex filament of finite core performed by Widnall[4] and referred to earlier in terms of its approach to eliminating the self-induction singularity, corrected the earlier work. A comparison of the divergence rates predicted by the present study with those predicted by Widnall shows close agreement for the core size = 0.1, while the results are significantly different for core size = 0.33. This presumably is because such large core sizes can accurately be treated by matched asymptotic expansion at the singularities. In practical cases, the core size seldom exceeds 0.1 and for core sizes up to 0.1 using matched asymptotic expansions against simple modification of the denominator for removing singularities does not provide with any appreciable improvement in accuracy.

Another special case of special interest is the S. C. Crow analysis of the stability of a pair of straight parallel vortices as trailed from a fixed wing aircraft. If the limiting value of pitch tending to infinity is taken in the present study for the case of a two-bladed rotor, that wake should correspond to two straight, parallel infinite vortices. The limiting process and comparisons of the formulations which results in each study are described in Appendix I and Sec. 4.6 of Ref. 5; a one-to-one correspondence is shown.

Most of the results for multibladed rotors are obtained for pitch = 0.1 and a core size = 0.1. A few cases were also run for pitch = 0.15 and core size = 0.33. Stability is adversely affected by decreasing pitch, apparently the stronger interaction between adjacent coils at lower pitch values accentuates unstable trends. The same can be said for core size, since the smaller the core the higher the maximum induced velocities that are experienced. The effect of core size on stability, however, is less marked for multiple helices. When the core size was increased from 0.10 to 0.33, the amplification rate dropped only about 2% for the wave number with highest divergence rates in all multiple bladed rotor cases. However, the core size does appear to be an important influence on the stability of a single helix.

For a two-bladed rotor minima occur at half odd integer wave numbers. For large wave numbers, i.e., short wavelength perturbations, the difference between maximum and minimum divergence rates decreases. The stability results for three-, four-, five-, and six-bladed rotors exhibit similar divergence rate and wave number relationship; i.e., the maximum and minimum divergence rates occur at wave numbers equal to $\frac{1}{2}$ times integer multiples, respectively, times the number of blades. For example, for a three-bladed rotor maxima occur at wave numbers 1.5, 3.0, and 4.5 etc., while the minima occur at wave numbers 0.75, 2.25, and 3.75 etc. For three-, four-, five-, and six-bladed rotors the excursion from the mean divergence rates also decreases with increasing wave numbers. Enveloping curves can be drawn through maxima and minima points in all cases. There is some absolute maximum divergence rate which occurs at the maximum of the enveloping curve. For two-, four-, and six-bladed rotors this absolute maximum divergence rate occurs at wave number 0.0, i.e., for the dilatational mode. For three- and five-bladed rotors the dilatational mode is still highly unstable, but the absolute maximum divergence rate occurs at

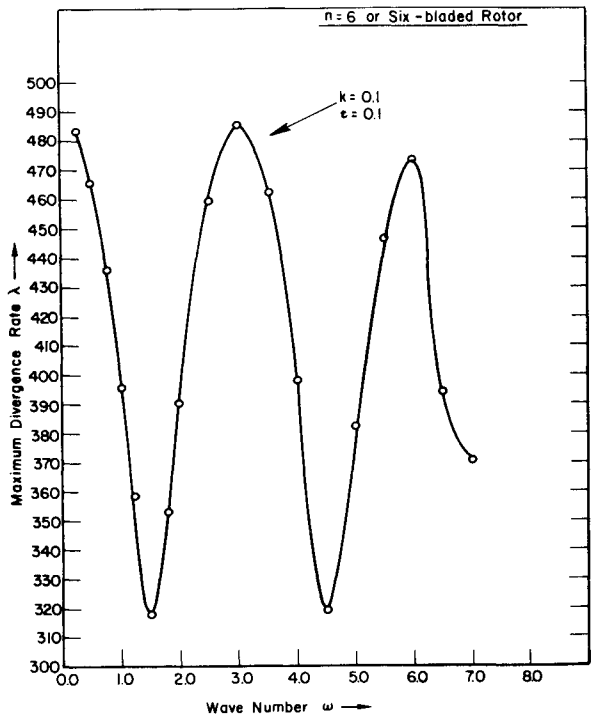

Fig. 8 Plot of maximum divergence rate vs wave number for six-bladed rotor.

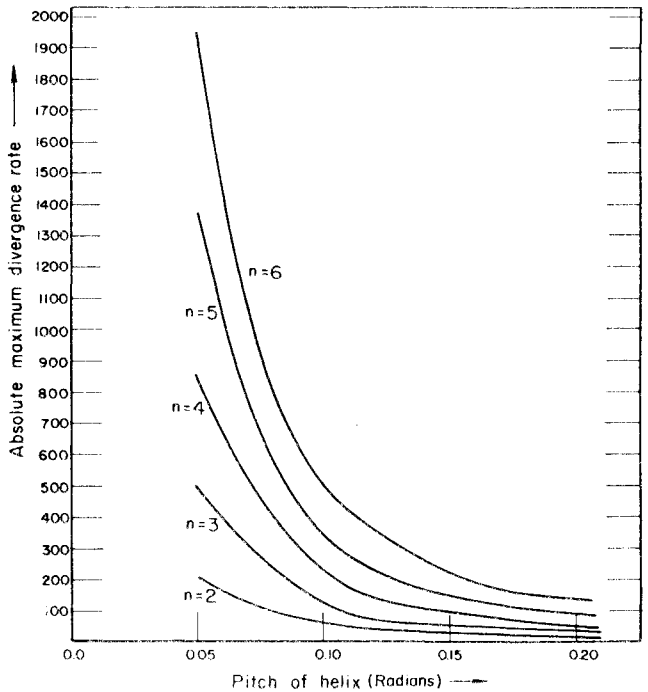

Fig. 9 Absolute maximum divergence rates for multibladed rotors of varying pitch.

wave numbers 1.5 and 2.5, respectively, i.e., where the wave number is one half the number of blades. As noted earlier the divergence rates vary with helix pitch; the absolute maximum divergence rate variation with helix of pitch is plotted in Fig. 9 for rotors with various numbers of blades.

The nondimensional divergence rate of multiple bladed rotors seems to increase with the number of blades for the same sort of reason that it increases with decreasing pitch; namely decreased spacing between adjacent coils of the vortices. In terms of the stability of the vortex for rotors of equal lifting capacity, even when the dimensionality is reinserted, i.e., accounting for the higher value of Γ which is involved, the fewer blades the better.

There is very little in the form of the experimental evidence against which to check the predictions made in the present investigation of wake stability. However, some qualitative experimental results have been reported by Landgreve[1] and the flow visualization data given there leads to the qualitative conclusion that the far wake region of a hovering rotor is unstable or, at best, neutrally stable.

After the conclusion of the research reported here, recent experimental work by Tangler, Wohlfeld, and Miley[10] came to the authors' attention. Reference 10 reported experimental investigations of vortex stability and noise for hovering model rotors including the effect of the tip shapes and compressibility. Among other things, the number of blades, collective pitch, and tip speed were varied. In every case, whenever the axial separation between vortices was reduced by various combinations of these rotor parameters, the vortices were found to become more unstable and were seen to diffuse sooner. The experimental conclusions follow the trends predicted by the present work.

Conclusions

In summary, helical vortex divergence rates are most unstable in deformation modes where axial separation between segments of vortices at the same circumferential position (either on adjacent helices or on adjacent coils on the same helix) are affected most and where the arc lengths so involved are longest. Conversely, the divergence rates are least where such axial separation is affected the least. The effect of radial or circumferential deformations seems to be unimportant in comparison to the axial deformations. As would be expected, then, maximum divergence rates in the unstable modes increase as the helical pitch decreases, increase as the number of helices increase, and decrease as the number of cycles of deformations in one turn of the helix (i.e., wave number) increases.

References

[1] Landgrebe, A. J., "An Analytical Method for Predicting Rotor Wake Geometry," *Journal of American Helicopter Society*, Vol. 14, No. 4, Oct. 1969, pp. 20–32.

[2] von Kármán, T., *Aerodynamics*, Cornell Univ. Press, Ithaca, N.Y., 1954, pp. 31–59.

[3] Levy, M. A. and Forsdyke, A. G., "The Steady Motion and Stability of a Helical Vortex," *Proceedings of the Royal Society*, Vol. 120, No. A786, Oct. 1, 1928, pp. 670–690.

[4] Widnall, S. E., "The Stability of a Helical Vortex Filament," *Journal of Fluid Mechanics*, Vol. 54, Pt. 4, 1972, pp. 641–663.

[5] Gupta, B. P. and Loewy, R. G., "Analytical Investigation of the Aerodynamic Stability of Helical Vortices Shed From a Hovering Rotor," USAAMRDL TR-73-84, Oct. 1973, University of Rochester, Rochester, N.Y.

[6] Batchelor, G. K., *An Introduction to Fluid Dynamics*, Cambridge Univ. Press, Cambridge, England, 1967, p. 264.

[7] Crow, S. C., "Stability Theory for a Pair of Trailing Vortices," *AIAA Journal*, Vol. 8, No. 12, Dec. 1970, pp. 2172–2179.

[8] Acton, F. S., *Numerical Methods That Work*, Harper and Row, New York, 1970, p. 347.

[9] Thomson, W., "On the Vibrations of a Columnar Vortex," *Philosophical Magazine*, Serial 5, Vol. 10, No. 61, Sept. 1880, pp. 155–168.

[10] Tangler, J. L., Wohlfeld, R. M., and Miley, S. J., "An Experimental Investigation of Vortex Stability, Tip Shapes, Compressibility and Noise for Hovering Model Rotors," CR-2305, Sept. 1973, NASA.